

Check for updates

Comprehensive Si Anode Design for Sulfide-Based all-Solid-State Batteries: Insights into Si-Electrolyte Synergy for Mitigating Contact Loss

Youngjin Song, Sungjin Cho, Suhwan Kim, Youyeong Shin, Ikcheon Na, Jongwoo Lim, Yong Min Lee,* and Soojin Park*

All-solid-state batteries (ASSBs) are emerging as a promising alternative to conventional lithium-ion batteries, offering improved safety and potential for energy density. However, the substantial volume fluctuations of high-capacity anodes such as lithium and silicon induce interfacial degradation, impeding practical applications. Herein, an aluminum-silicon (Al-Si) alloy anode is introduced that effectively mitigates these challenges by stabilizing volume variation after initial volume expansion and maintaining stable interfacial integrity with the solid electrolyte (SE). By employing a SE-free wet anode and leveraging advanced characterization techniques, including three-dimensional X-ray nanoimaging and digital twin-based particle-to-electrode volume expansion simulations, the structural evolution and electrochemical behavior of Al-Si are elucidated. Furthermore, the integration of an elastic-recoverable anolyte enables the formation of a robust Al-Si composite anode, effectively suppressing contact loss and enhancing reversibility. ASSBs integrating this Al-Si composite anode and a high-areal-capacity LiNi_{0.8}Co_{0.1}Mn_{0.1}O₂ cathode (6 mAh·cm⁻²) achieve a capacity retention of 81.6% after 300 cycles, offering a viable pathway toward high-energy-density and durable ASSBs.

1. Introduction

All-solid-state batteries (ASSBs) based on sulfide solid electrolytes (SSEs) have garnered significant attention as

next-generation energy storage systems owing to their potential to overcome the safety limitations of conventional lithiumion batteries (LIBs) while offering potential for high energy density. Unlike the flammable liquid electrolytes (LEs) used in LIBs, SSEs offer superior thermal stability and mechanical robustness. A critical factor in maximizing the energy density of ASSBs is the choice of anode material. While graphite, with a theoretical capacity of 372 mAh g⁻¹, has been used as primary anode material in LIBs, its low-capacity limits further energy density enhancement.

To address this, high-capacity anodes such as lithium (Li) metal and silicon (Si), with theoretical capacities of 3860 and 3590 mAh g⁻¹ respectively, have been investigated.^[6] However, both materials encounter challenges due to substantial volumetric changes during cycling. Li metal is highly reactive and prone to dendrite growth and interfacial instability, while Si

undergoes >300% volume expansion upon lithiation, leading to pulverization, contact loss, and compromised electrochemical instability as shown in **Figure 1a.**^[7,8] These issues are further

Y. Song, S. Cho, S. Park
Department of Chemistry
Pohang University of Science and Technology (POSTECH)
Cheongam-ro 77, Nam-gu, Pohang 37673, Republic of Korea
E-mail: soojin.park@postech.ac.kr

S. Kim, Y. M. Lee

Department of Energy Science and Engineering
Daegu Gyeongbuk Institute of Science and Technology
Techno jungang-daero 333, Dalseong-gun, Daegu 42988, Republic of Korea
E-mail: yongmin@yonsei.ac.kr

The ORCID identification number(s) for the author(s) of this article can be found under https://doi.org/10.1002/adfm.202504739

© 2025 The Author(s). Advanced Functional Materials published by Wiley-VCH GmbH. This is an open access article under the terms of the Creative Commons Attribution-NonCommercial License, which permits use, distribution and reproduction in any medium, provided the original work is properly cited and is not used for commercial purposes.

DOI: 10.1002/adfm.202504739

Y. Shin, Y. M. Lee

Department of Battery Engineering

Yonsei University

Yonsei-ro 50, Seodaemun-gu, Seoul 03722, Republic of Korea

I. Na, J. Lim

Department of Chemistry

Seoul National University

Gwanak-ro 1, Gwanak-gu, Seoul 08826, Republic of Korea

Y. M. Lee

Department of Chemical and Biomolecular Engineering

Yonsei University

Yonsei-ro 50, Seodaemun-gu, Seoul 03722, Republic of Korea

16163028, 2025, 43, Downloaded from https://advanced.onlinelibrary.wiley.com/doi/10.1002/adfm.202504739 by Daegu Gyeongbuk Institute Of, Wiley Online Library on [03/12/2025]. See the Terms

and-conditions) on Wiley Online Library for rules of use; OA articles are governed by the applicable Creative Common

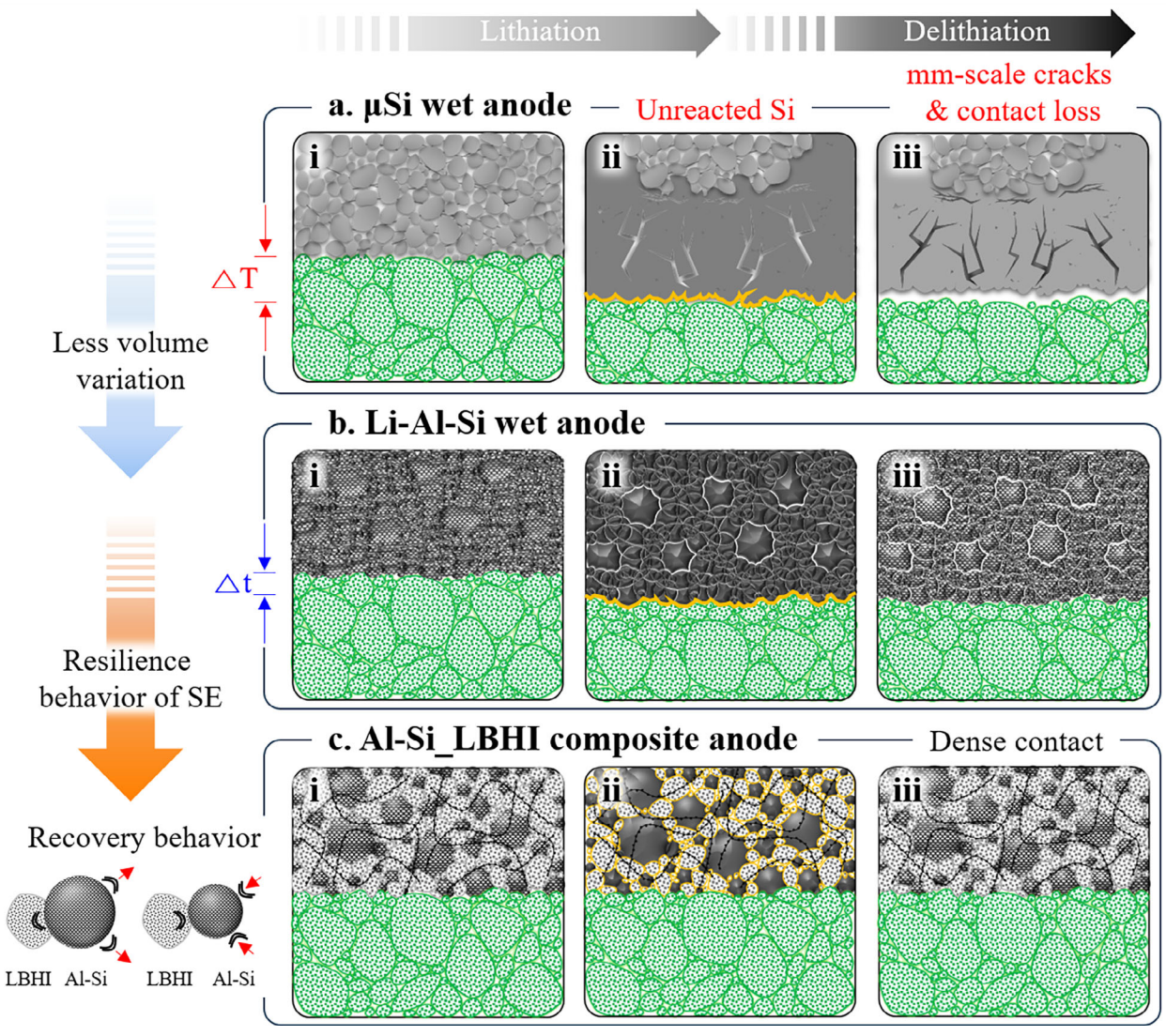


Figure 1. Design strategies for stable, high-loading Si-based anodes. a) SE-free μSi wet anode. b) SE-free Li-Al–Si wet anode featuring Al incorporation and prelithiation to enhance 2D interfacial stability and minimize volume change. c) Al–Si_LBHI composite anode with anolyte showing elastic recovery behavior, enabling 3D contact during cycling: i) as-pressed (post-assembly), ii) SOC 100% (fully lithiated), and iii) SOD 100% (fully delithiated), illustrating structural evolution and interfacial stability.

exacerbated in ASSBs, where the rigidity of SSEs amplifies mechanical stress at the electrode interface. [9]

Micron-sized Si (μSi) has emerged as a promising anode for ASSBs due to its low cost, natural abundance, and environmental compatibility.^[10] In contrast to LEs, SSEs are less likely to infiltrate porous Si electrodes, thereby mitigating dynamic solid electrolyte interphase (SEI) formation—a key degradation mechanism in conventional systems.^[11] Nonetheless, the practical implementation of Si in ASSBs remains limited by issues such as particle pulverization, stress-induced fracture, and its inherently low electronic conductivity.^[12] To overcome these limitations, various strategies have been explored, including particle size control, surface engineering, and the incorporation of carbon-based materials with reduced volume change.^[5,13–16] Additionally, prelithiation techniques—including electrochemical, chemomechanical, and thermochemical approaches—have been developed to

suppress volume expansion and enhance the rate performance of Si-based electrodes. [17–20] There have also been attempts to utilize lithium silicide as a lithiophilic site with proper hardness after prelithiation rather than as the main active material. [21–23] However, these approaches often introduce complexity, increase cost, and pose challenges for scalability, thereby hindering the commercialization of Si-based ASSBs. Similar concerns have been raised for other alloy-based anodes, where interfacial instability with the SSE layer due to stress accumulation remains a critical challenge. [24,25]

In this context, aluminum–silicon (Al–Si) alloys have attracted attention as an alternative active material for ASSBs. Al offers a theoretical capacity of 990 mAh g⁻¹ via the formation of the β -LiAl phase and exhibits significantly lower volume expansion (\approx 96%) than Si.^[26] Additionally, its high electronic conductivity eliminates the need for conductive additives, which are known to



www.afm-journal.de

trigger parasitic reactions with SSEs.^[10,12] Furthermore, the rigid framework provided by Si and the ductile matrix provided by Al enhance the structural stability of the Al–Si particle during lithiation, mitigating contact loss and enhancing cycle stability.^[27–30] Consistently, structural-mechanical simulations reveal that during lithiation, Al and Si undergo localized strain that promotes internal structural accommodation and preserves electrode integrity.

The Al–Si wet anode (sAl–Si) also exhibits unique volumetric behavior: volume expansion reaches saturation near 30% state of charge (SOC) during the first lithiation. Notably, minimal volume contraction occurs upon delithiation, with a slight expansion observed instead. This exceptional volumetric stability plays a key role in mitigating contact loss — a critical degradation factor in Si-based ASSBs. An electrochemical prelithiation process was employed to leverage this property, inducing volume expansion prior to cell assembly. The resulting prelithiated Al-Si anode (sLi-Al-Si) showed a reduced volume variation of ≈37.5% (Figure 1b), significantly lower than that of pristine sAl-Si and sµSi. In full-cell tests paired with NCM811 dry cathodes (NCM loading level of 8.2 mg·cm⁻²), the sLi-Al-Si delivered over 100 mAh g⁻¹ for more than 250 cycles, confirming excellent stability. Advanced characterization tools—including in situ stress monitoring, synchrotron-based 2D/3D X-ray nanoimaging, and simulations—were employed to elucidate the origins of the exceptional stability of the Al-Si anode.

To enable high-loading anode operation while maintaining interface integrity, a composite anode structure was designed by integrating a hydride-based SE (3LiBH₄–LiI, LBHI) as an anolyte. The anolyte establishes a 3D interfacial architecture with the active material, alleviating contact degradation typically observed at planar anode/SSE interfaces. In addition to its recently acknowledged electrochemical stability under low potentials, ^[31] LBHI exhibits elastic recovery behavior—identified in this work—which helps accommodate stress during cycling and supports long-term mechanical resilience. While compatibility between cathode materials and catholytes has been widely studied, analogous understanding for anode/anolyte interfaces remains limited. ^[20,32]

This study identifies key factors for designing stable composite anodes in ASSBs. While $\rm Li_6PS_5Cl$ (LPSCl) offers high ionic conductivity, its interfacial reactivity with Si and irreversible plastic deformation limit long-term cycling. In contrast, LBHI demonstrates superior mechanical resilience and interfacial compatibility with Al–Si, maintaining dense contact and reducing interfacial resistance (Figure 1c). A full cell with a high areal-capacity NCM811 cathode (6 mAh-cm $^{-2}$) and a composite Al–Si anode exhibited 81.6% capacity retention after 300 cycles and $\approx\!70\%$ after 500 cycles, highlighting the practical viability of this design. This work represents the first demonstration of an Al–Si anode in sulfide-based ASSBs and offers a simple, scalable strategy toward high-performance solid-state energy storage.

2. Results and Discussion

2.1. Characterization of SE-Free anodes and Electrode-Level Behavior Analysis

The Al–Si and μSi wet anodes, fabricated via a slurry casting process, were denoted as sAl–Si and s μSi , respectively. The areal

loadings were 2.15 $mg_{Al-Si} \cdot cm^{-2}$ for sAl–Si and 0.88 $mg_{\mu Si} \cdot cm^{-2}$ for sµSi, both composed of 99 wt.% active material and 1 wt.% poly(vinylidene fluoride) (PVDF) binder.

To evaluate electrical conductivity, sheet resistance measurements were conducted using a four-point probe (Figure S1a, Supporting Information). As the Si content increased in the Al-Si composition, the sheet resistance also increased, indicating decreased electrical conductivity (Figure S1b, Supporting Information). The sAl-Si anode exhibited sheet resistance comparable to that of Ni foil and significantly higher conductivity than sµSi. These results suggested a viable strategy to enhance the conductivity of Si-based anodes without incorporating carbon additives, which could induce side reactions with SSEs.[10] Nanoindentation tests on pelletized active materials revealed that the high ductility of Al-Si contributed to maintaining stable and intimate contact with the SSE throughout repeated volume changes (Figure S2a,b, Supporting Information). However, Si showed minimal deformation, indicative of its brittle nature. A comparative analysis of hardness and elastic modulus showed a progressive increase in the order of Al, Al-Si, and Si (Figure S2c,d, Supporting Information), which likely influenced the internal structure of the anode after cell assembly.

Internal electrode morphology was examined using nano-computed tomography (nCT), focused ion beam (FIB), and scanning electron microscopy (SEM) on cells after disassembly. The ductile nature of sAl−Si led to substantial particle deformation under ≈500 MPa uniaxial pressure during assembly, as revealed by nCT images acquired via synchrotron radiation (Figure 2a). In the as-pressed state, sAl−Si exhibited a somewhat uneven morphology with visible grains, likely due to the relatively large particle sizes compared to the electrode thickness, as shown in the SEM image (Figure S3a, Supporting Information). The distorted particles formed dense contact, minimizing interparticle pores. Additionally, the internal structure within individual particles—comprising a Si skeleton embedded in an Al matrix—was revealed in cross-sectional images obtained after FIB milling (Figure S4a, Supporting Information).

Conversely, sµSi retained its particle morphology under the same pressure and maintained high interparticle porosity, as observed in Figure 2b and Figure S4d (Supporting Information). This contrast in structural response indicated that sAl–Si formed a compact network, while sµSi preserved its porous character due to its rigidity. Porosity calculations based on areal loading, composition, and post-assembly thickness showed values of 4.67% for sAl–Si and 43.53% for sµSi (Table S1, Supporting Information).

To analyze structural evolution during cycling, cross-sectional images were collected at various SOC using half-cells with Li metal (Figure 2c,d). The five stages—i) as-pressed, ii) SOC 50%, iii) SOC 100%, iv) state of discharge (SOD) 50%, and v) SOD 100%—were marked on the voltage profile. Both anodes achieved similar areal capacities (\approx 2.7–2.8 mAh·cm⁻²) and initial coulombic efficiencies (ICEs) of 67.2% and 65.0%, respectively.

Upon cycling, the sAl–Si surface became smoother, and visible grains disappeared (Figure S3b,c, Supporting Information). In cross-section, mismatched volumetric expansion between Al and Si caused deformation in the internal structure (Figures S4b,c, S5a,b, and S6a,b, Supporting Information). In sµSi, lithiation caused Si softening and the merging of particle boundaries, consistent with previous studies. $^{[10,12,13,21,23]}$ In addition to vertical

16163028, 2025, 43, Downloaded from https://advanced.onlinelibrary.viley.com/ob/10.1002/adfm.202040730 by Daegu Gyeongbuk Institute Of, Wiley Online Library on [03/12/2025]. See the Terms and Conditions (https://onlinelibrary.wiety.com/terms/

and-conditions) on Wiley Online Library for rules of use; OA articles are governed by the applicable Creative Commons

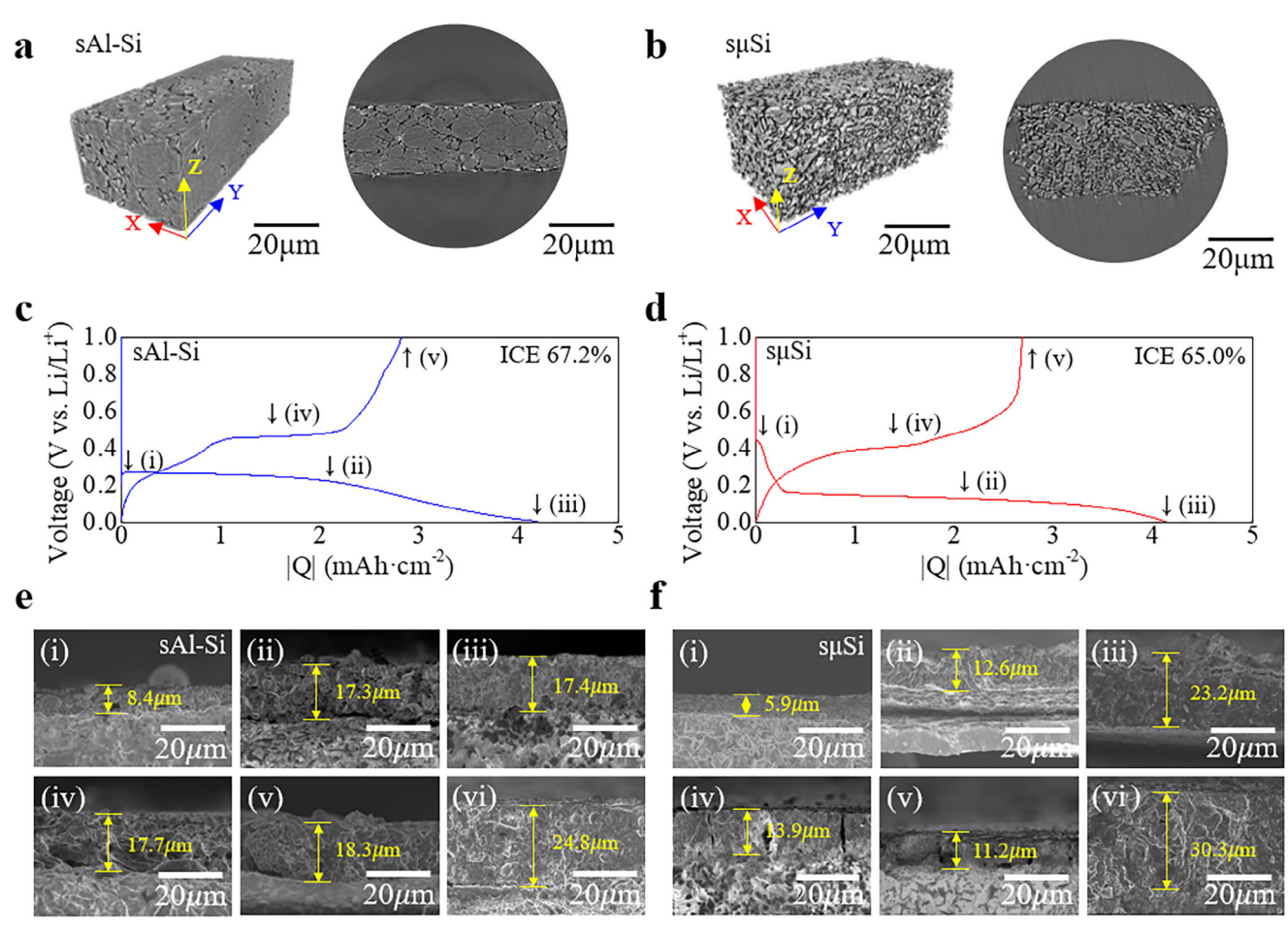


Figure 2. Multiscale characterization of the Si-based electrodes within ASSBs. 2D/3D nCT images of a) sAl-Si and b) sµSi acquired via synchrotron radiation revealing detailed internal structure. Voltage profiles of Li metal half-cells with c) sAl-Si and d) sµSi. Cross-sectional SEM images of e) the sAl-Si and f) sµSi anodes at various state-of-charge (i-v) as indicated in the voltage profiles (c,d) and after 30 cycles (vi).

cracks, small horizontal cracks also formed (Figures S3e, S4e, and S5c, Supporting Information), which likely led to electrically isolated Si regions and irreversible capacity loss. These horizontal cracks persisted during delithiation (Figures S3f, S4f, and S5d, Supporting Information), suggesting substantial mechanical stress and instability driven by the large volume changes of Si.

It is important to note that FIB and nCT imaging were conducted after disassembling the cells without applied stack pressure. This may have altered the observed morphology compared to the actual operando state. Therefore, simulations were needed to better understand the volumetric evolution of the sAl-Si anode and the associated chemo-mechanical interactions.

The electrode thickness change over cycling was quantified via cross-sectional SEM (Figure 2e,f). The initial thickness of sAl-Si (8.4 µm) increased to \approx 16.6 µm at SOC 30% (Figure S7, Supporting Information), followed by slight additional swelling during the initial cycle (Figure 2e). After 30 cycles, the thickness increased by ≈200%, attributed to the combined effect of the Al matrix^[26] and the Si framework.

In contrast, sµSi expanded from 5.9 to ≈23.2 µm at SOC 100% (Figure 2f). At SOD 100%, the thickness dropped to less than half the maximum value, causing contact loss at the anode-SE interface. After 30 cycles, suSi exhibited over 400% expansion, accompanied by numerous vertical cracks, which were commonly reported for bare Si anodes.[10,13]

To further assess interface resistance evolution, electrochemical impedance spectroscopy (EIS) was performed with NCM full cells (Figure S8, Supporting Information). sµSi displayed poor interfacial contact in both the as-pressed and fully delithiated states, as indicated by the lack of a clear intercept on the Nyquist plot and higher interfacial resistance compared to sAl-Si. The poor contact was attributed to the inherent rigidity of Si and its substantial volume fluctuations during cycling.

Raman and X-ray diffraction (XRD) analyses were performed to investigate phase reversibility in the anodes (Figure S9, Supporting Information). For sAl-Si, the Raman spectrum showed a crystalline Si peak at 518.9 cm⁻¹ before cycling. After full lithiation, a new Li_xSi_y peak appeared at 425.8 cm⁻¹, and the Si peak disappeared. Úpon delithiation, the crystalline Si peak reappeared at 512.9 cm⁻¹, confirming reversible alloying. XRD patterns revealed Al peaks at 38.7°, 44.9°, and 78.3°, which disappeared upon lithiation and were replaced by peaks from Li_xSi_{1-x} and Li_vAl_{1-v}. These peaks diminished upon delithiation, and the

1616308.2025, 43, Downloaded from https://advanced.onlinelibrary.wiley.com/doi/10.1002/adrifi.20254739 by Daegu Gyeongbuk Institute of, Wiley Online Library on [03/122025]. See the Terms and Conditions (https://onlinelibrary.wiley.com/terms-and-conditions) on Wiley Online Library for rules of use; OA articles are governed by the applicable Certain Common.

www.afm-journal.de

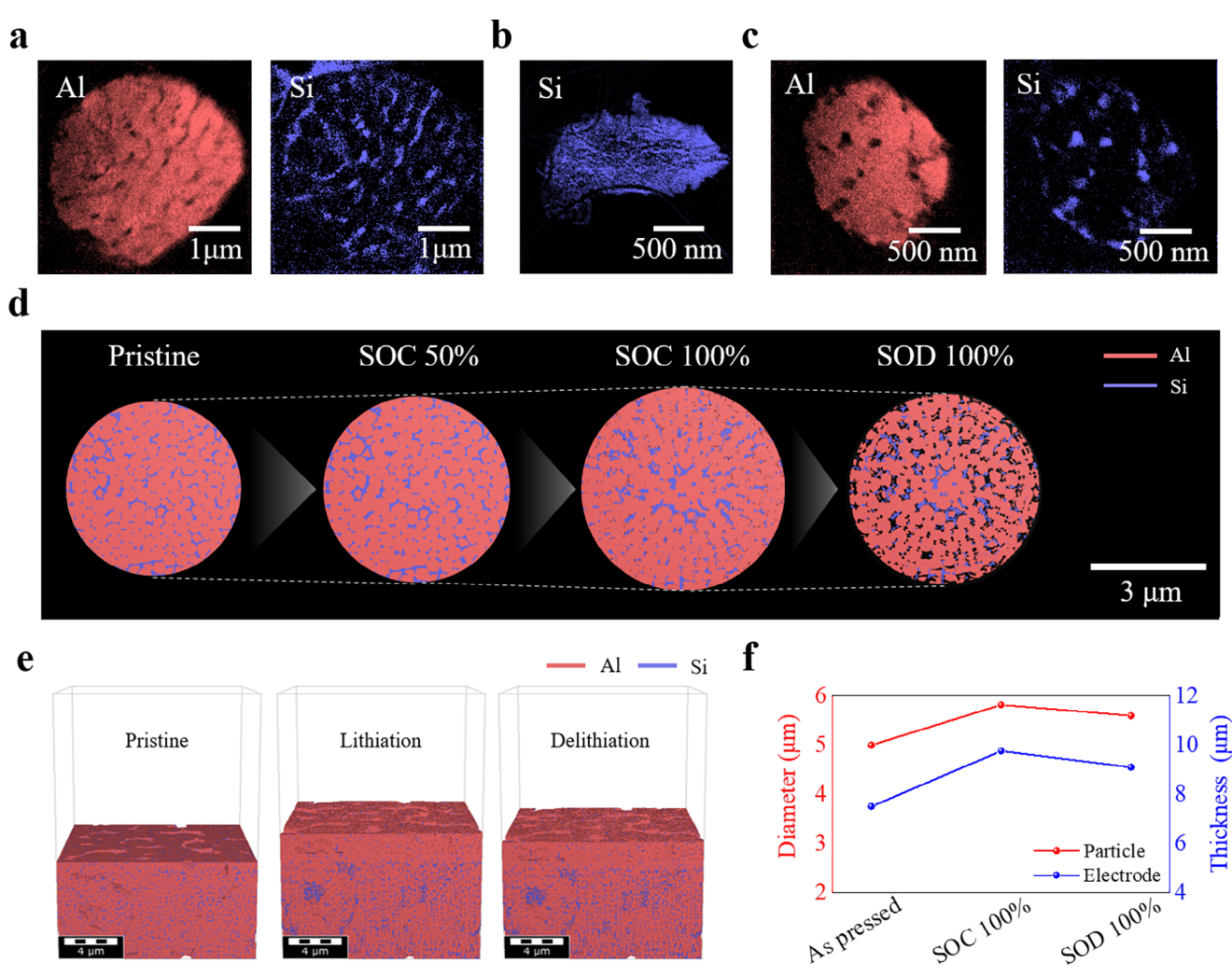


Figure 3. Microstructural characterization and digital twin simulations. a-c) EELS mapping of Al-Si, μSi, and Li-Al-Si showing the spatial distribution of key elements. d,e) Digital twin simulations of microstructural and volumetric evolution of Al-Si at the particle scale and electrode scale during the first cycle. f) Simulated changes in particle diameter and electrode thickness.

original Al peaks re-emerged. In sµSi, a sharp Si peak at 523.5 cm⁻¹ was observed in the Raman spectrum before lithiation, which disappeared after lithiation. The post-delithiation spectrum showed a broadened, downshifted peak at 503.8 cm⁻¹, suggesting partial amorphization. XRD patterns confirmed the disappearance of Si peaks during lithiation and emergence of Li, Si_{1-v} peaks. Upon delithiation, the Si peaks did not fully recover, indicating irreversible structural changes.

2.2. Characterization of Active Materials and Simulation of **Volumetric Change Behavior**

Comprehensive structural and compositional characterizations were conducted to simulate the charge-discharge behavior of active materials at the particle level. The internal structure of Al–Si particles was analyzed using transmission electron microscopy (TEM) after FIB milling (Figure S10, Supporting Information). Cross-sectional TEM revealed that Si is embedded within the Al matrix as a complex, interconnected network, as confirmed by electron energy loss spectroscopy (EELS) mapping (Figure 3a). In contrast, µSi particles displayed a simpler structure, with Si uniformly distributed (Figure 3b). Lithiated Al-Si (Li-Al-Si) particles were prepared by contacting Al-Si particles with molten Li at 300 °C in an Ar-filled glovebox (Figure \$11, Supporting Information). FIB-milled samples showed that lithiation caused partial phase segregation, with Si forming agglomerates in the Al matrix (Figure 3c). This redistribution likely stems from differences in lithiation dynamics between Al and Si, which may influence the mechanical and electrochemical properties of the lithiated particles. To further probe the internal structure of Al-Si, selective etching of Al using hydrochloric acid was performed (Figure S12a, Supporting Information). Energy-dispersive spectroscopy (EDS) areal scans confirmed a progressive decrease in the Al:Si weight ratio over time (Figure S12b, Supporting Information). After 6 h of etching, particle fragmentation was observed due to matrix dissolution. After 8 h, most Al was removed, leaving behind a porous Si framework (Figure S12c,



www.afm-journal.de

Supporting Information).^[27,33–36] This transformation reflects the eutectic microstructure of the alloy, composed of 88 wt.% Al and 12 wt.% Si.^[37]

XRD analysis (Figure S12d, Supporting Information) showed that Al–Si powders contain Al peaks at 38.2°, 44.5°, 65.0°, and 78.1° ((111), (200), (220), and (311), respectively), [^{26,38]} and Si peaks at 28.2°, 47.0°, and 55.8° ((111), (220), and (311), respectively). [^{5,6,10,21,31]} Compared to μ Si, Si peaks in Al–Si were shifted by 0.15–0.35°, suggesting residual strain. After 9 h of etching, Al peaks nearly disappeared, and the XRD pattern resembled that of μ Si.

High-resolution TEM revealed lattice fringes corresponding to Al (111) and Si (111) planes with d-spacing values of 0.23 and 0.32 nm, respectively (Figure S13a, Supporting Information). Fast Fourier transform and selected area electron diffraction confirmed the presence of both phases and indicated phase separation (Figure S13b–d, Supporting Information). [33,39,40]

Simulating the volumetric change behavior of anodes during electrochemical cycling offers valuable insights into the mechanisms impacting electrode performance and structural stability. Figure 3e,f illustrate the key considerations and procedural steps involved in performing such simulations. These simulations enable detailed analysis of mechanical stresses, structural deformations, and their effects on the structural integrity of the anode material, providing a foundation for optimizing material design and cycling performance. Using the aforementioned structural information, a virtual Al-Si structure was constructed based on the measured morphology (Figure \$14a,b, Supporting Information). Based on this structure, a volume expansion simulation was performed at the particle-level, incorporating mechanical properties such as modulus and failure stress for each material (Table S2, Supporting Information). [41,42] Upon lithiation, the particle is expanded by ≈16% in diameter and ≈58% in volume, with Si expansion exceeding 300%, reaching the failure stress threshold and leading to Si skeleton fracture (Figure S14c,d, Supporting Information). Upon delithiation, only a 4% diameter reduction was observed, and the Si framework remained largely intact (Figure 3d), suggesting that initial deformation stabilizes the particle structure during cycling. This suggests that the initial deformation of the Si skeleton plays a crucial role in preserving the structural integrity of the Al-Si particle under continuous cycling.

Furthermore, a volume expansion simulation was conducted at the electrode-level (Figure 3e). During the initial volume expansion, the calculated sAl–Si thickness increased by ≈30%, exhibiting Si agglomeration similar to experimental results shown in Figure 3c. Despite this structural evolution, the anode maintained good interparticle connectivity and conduction pathway (Figure \$15, Supporting Information). In contrast, at the delithiation state, the calculated thickness decreased by only 7%, a ratio comparable to that observed at the particle-level (Figure 3f). Meanwhile, the sµSi structure exhibited a large thickness increase of 47% in the lithiation process, returning to a thickness close to its initial state upon delithiation (Figure \$16, Supporting Information). Through these digital twin-based volume expansion simulations from the particle to the electrode-level, the mechanism of sAl-Si structural integrity was reliably proposed as a point of the structural-mechanical changes of sAl-Si. These results highlight the structural stability of sAl-Si across multiple scales, enabled by its alloy microstructure.

2.3. The Li-Al-Si Anode Fabrication via the Prelithiation Process

The volumetric expansion behavior of sAl–Si during cycle indicates that most of its expansion occurs during the initial stages of lithiation. This suggests that a prelithiation step prior to cell assembly could enhance structural stability over extended cycles. Prelithiated electrodes undergo less expansion during subsequent cycles, minimizing interfacial detachment in ASSBs. Additionally, prelithiation reduces first-cycle irreversible losses—such as those due to SEI formation—thereby improving the ICE.

Prelithiation was carried out in a dry room using a two-electrode setup with Li metal as the counter electrode and liquid electrolyte (Figure S17, Supporting Information). sAl–Si electrodes (9 cm \times 9 cm) were prelithiated to a 30% state of charge (SOC), a value selected to balance ICE and volume stability. Assuming a capacity of 4 mAh·cm $^{-2}$ and applying a current density of 0.1 C (0.4 mA·cm $^{-2}$), the prelithiation process lasted 200 min. (**Figure 4a**). The electrode composition was adjusted to 90 wt.% Al–Si, 5 wt.% vapor-grown carbon fiber (VGCF), and 5 wt.% PVDF for compatibility with the liquid electrolyte. The resulting prelithiated electrode is referred to as sLi–Al–Si.

EIS curves showed that sLi–Al–Si exhibited lower interfacial and charge-transfer resistance, as indicated by a reduced semicircle in the Nyquist plot (Figure 4b). Cross-sectional SEM images revealed that the surface of Al–Si particles became rougher after prelithiation, with electrode thickness increasing from 19 to \approx 26 µm (Figure 4c,d).

The volumetric changes during cycling are summarized in Figure 4e. Taking the post-assembly thickness as the 0% baseline, sµSi electrodes showed a 328% thickness increase after 10 cycles. In contrast, sAl–Si showed a 191% increase, which then stabilized. The sLi–Al–Si electrode demonstrated the most stable behavior, expanding only 93% over 10 cycles before reaching saturation. SEM images of full-cell cross-sections after 30 cycles (Figure S18, Supporting Information) also confirm that prelithiation effectively suppresses excessive expansion.

Full-cell tests using the NCM dry cathodes with NCM loading of 8.2 mg·cm⁻² demonstrated enhanced ICE as a result of prelithiation (Figure 4f). While sAl-Si and sµSi showed similar ICE values (64.4% and ≈61.5%), sLi-Al-Si achieved a significantly higher ICE of 84.7%. Under cycling conditions of 0.05 C (1 cycle), 0.1 C (3 cycles), and 0.2 C (subsequent cycles), sµSi showed rapid capacity degradation—falling to 60 mAh g⁻¹ by the 30th cycle—and a coulombic efficiency (CE) of 97.2% after 20 cycles (Figure 4g). sAl-Si exhibited improved stability, maintaining CE >99% for 20 cycles, though capacity declined to 60 mAh g⁻¹ by the 83rd cycle. In contrast, sLi-Al-Si achieved CE >99.2% from the second cycle and retained a capacity of 125 mAh g⁻¹ after 100 cycles, maintaining stable operation up to 290 cycles. For comparison, a NCM full cell using an In-Li anode was tested under identical conditions (Figure \$19, Supporting Information). Its capacity and volumetric energy density were lower than those of the sLi-Al-Si cell, owing to the use of a 100 μm In-Li foil along with an additional attached Li foil.

Surface morphology analysis after 10 cycles showed flat, crack-free surfaces in sLi–Al–Si and sAl–Si anodes (Figure S20a,b, Supporting Information), whereas s μ Si exhibited millimeter-scale cracks indicative of mechanical degradation (Figure S20c, Supporting Information). These observations reflect not only the

16163028, 2025, 43, Downloaded from https://advance-

onlinelibrary.wiley.com/doi/10.1002/adfm.202504739 by Daegu Gyeongbuk Institute Of, Wiley Online Library on [03/12/2025]. See the Terms and Conditions (https://onlinelibrary.wiley.com/ter

on Wiley Online Library for rules of use; OA articles are governed by the applicable Creative Commons

www.afm-journal.de

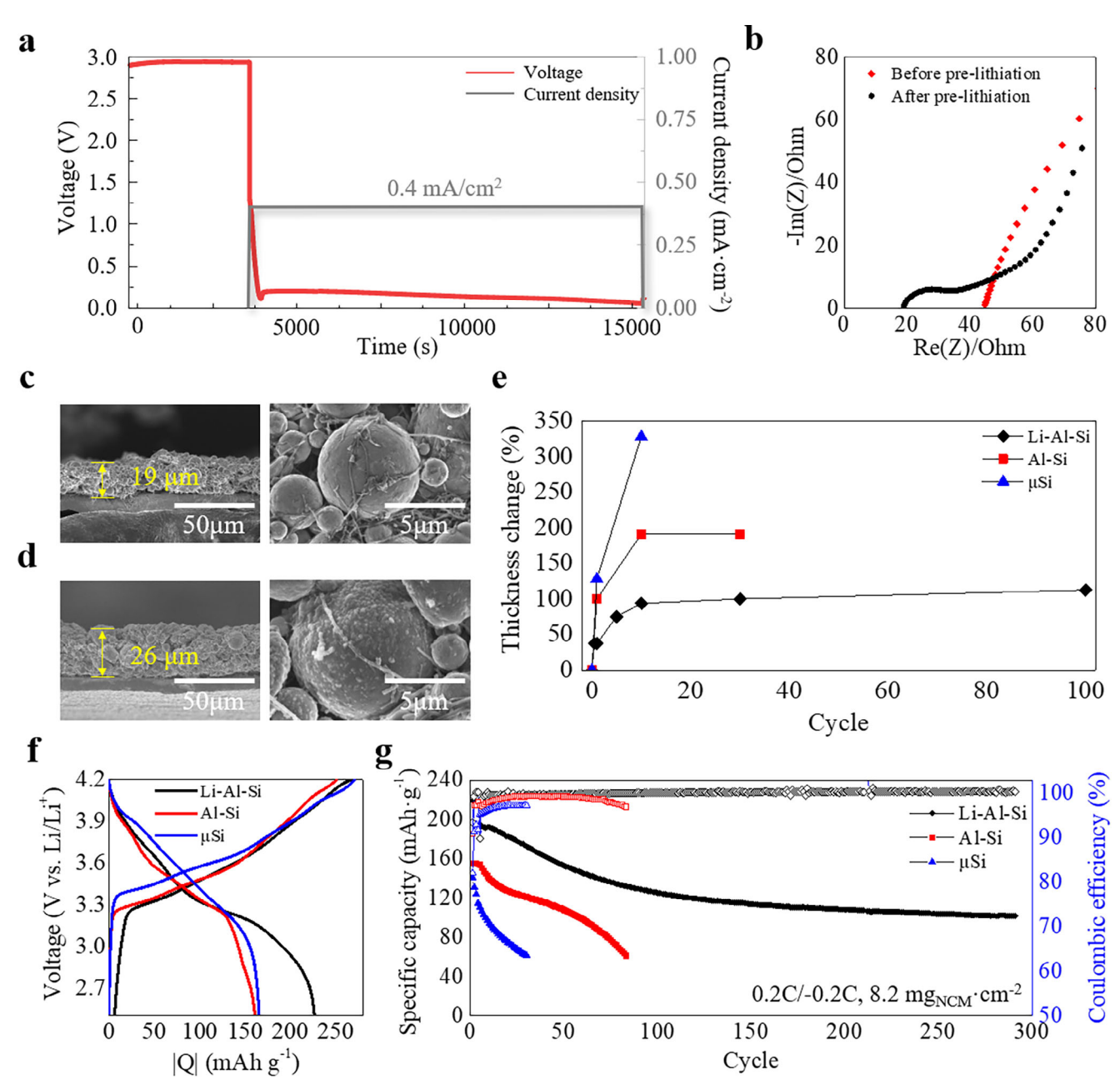


Figure 4. Electrochemical prelithiation process and its effects. a) Chronopotentiometric profile of the prelithiation process for Al–Si electrodes. b) EIS curves of Al–Si electrodes before and after prelithiation. c,d) Cross-sectional morphology of Al–Si electrodes before and after prelithiation. e) Electrode thickness variation ratio for various anode materials. f,g) Voltage profiles and long-term cycling performance of full cells with NCM811 dry cathodes.

intrinsic mechanical properties of the electrodes but also the reduced internal stress evolution associated with volume changes during cycling in ASSBs. To investigate the relationship between electrode thickness variation and stress evolution within ASSBs, in situ stress monitoring analysis was conducted using embedded sensors while cycling full cells at 0.1 C (Figure S21a–d, Supporting Information). Full-cell configurations with NCM cathodes were used to minimize the influence of counter-electrode volume changes, which are typically more pronounced in half-cell configurations. The pressure variation per delivered capacity was significantly lower in sAl–Si and even further reduced

in sLi–Al–Si (Figure S21e, Supporting Information), suggesting that prelithiation effectively mitigates volume-induced stress. X-ray photoelectron spectroscopy (XPS) analysis after 10 cycles (Figure S22, Supporting Information) revealed increased formation of Li–Al and Li–Si phases in the prelithiated Al–Si anode, contributing to reduced volume variation and enhanced structural stability. Notably, comparable levels of Li₂S were observed in both prelithiated and non-prelithiated samples, and the Cl 2p spectra did not show significant differences, indicating that pre-lithiation does not induce additional interfacial side reactions with the LPSCl electrolyte. Finally, post-mortem

16163028, 2025, 43, Downloaded from https://advanced.onlinelibrary.wiley.com/doi/10.1002/adfn.2025/4739 by Daegu Gyeongbuk Institute Of, Wiley Online Library on [03/12/2025]. See the Terms and Conditions (https://onlinelibrary.wiley.com/erms

and-conditions) on Wiley Online Library for rules of use; OA articles are governed by the applicable Creative Commons

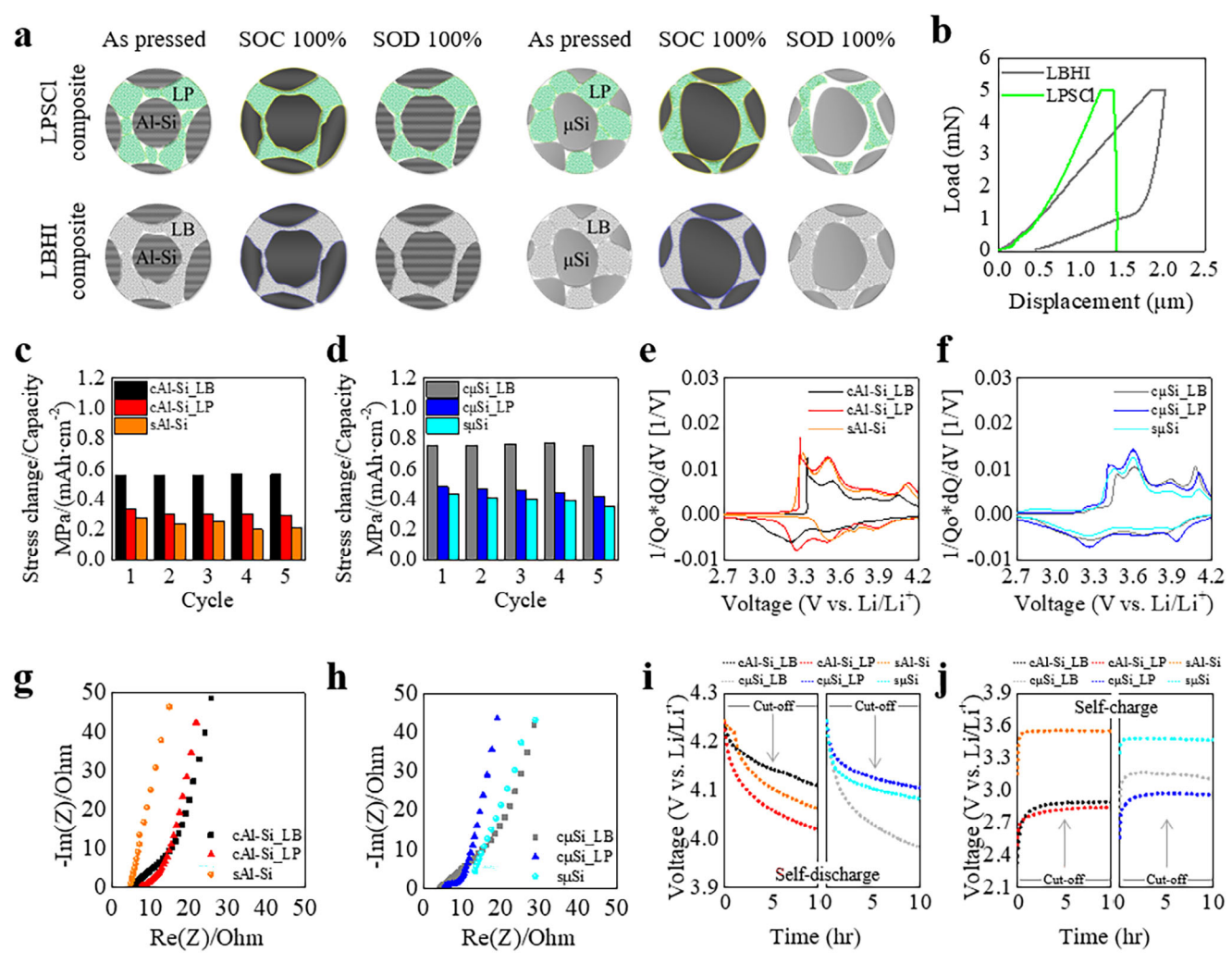


Figure 5. Comparability between SEs and active materials. a) Schematic of morphological behavior of active materials and SEs in composite anodes. b) Nanoindentation-based mechanical properties of SEs under vacuum. c,d) Internal stress distribution in NCM full cells with Al–Si and μSi anodes. e,f) dQ/dV curves of NCM full cells with Al–Si and μSi anodes (2.2–4.25 V). g,h) EIS spectra of Al–Si and μSi anodes after fabrication and 5 h of aging. i,j) Self-charge/discharge behavior of NCM full cells with Al–Si and μSi anodes.

reactivity tests were conducted by exposing the full cells to water after 30 cycles (Figure S23, Supporting Information). Both sLi–Al–Si and sAl–Si generated hydrogen gas upon water exposure, while sµSi reacted violently and ignited immediately upon contact with water, as reported in a previous study. Within 5 s, sµSi completely dissolved, leaving the electrolyte exposed. These results confirm the enhanced safety of the alloy-based anodes compared to pure Si.

2.4. Composite Anode Design: Correlation Between SEs and Active Materials

Even under the application of high stack pressure, significant limitations were observed in designing high-loading full-cells with SE-free wet anodes, even when employing the prelithiation process. To address these challenges, composite anodes incorporating SEs as anolytes offer a promising alternative. To identify the critical factors influencing the design of composite anodes, LPSCl and LBHI were selected as representative SEs, while μSi and Al–Si alloys served as active material candidates. VGCF and Super C65 were employed as conductive agents. Raman and XRD analyses confirmed the successful synthesis of the SEs and composite anodes without impurity formation (Figure S24 and S25, Supporting Information). The Raman spectra of LPSCl showed distinct PS $_4^{3-}$ vibrations, and its sharp XRD peaks indicated a highly crystalline structure. [47] In contrast, LBHI displayed broader diffraction features, suggesting a more amorphous nature. [31,48]

Figure 5a schematically illustrates the chemo-mechanical behavior of active materials and SEs during cycling. Al–Si particles in LPSCl-based composite anodes (cAl–Si_LP) exhibit voids at initial fabrication. Upon lithiation, Al–Si expands, plastically deforming the LPSCl and enhancing interfacial contact. However, delithiation leads to contact loss. Conversely, LBHI-based Al-Si anode (cAl–Si_LB) exhibits denser initial packing and





www.afm-journal.de

maintains contact throughout cycling due to LBHI's elastic recovery. For μSi , which undergoes larger volume changes, the benefits of LBHI diminish, and even with LBHI ($c\mu Si_LB$), stable contact cannot be maintained. Overall strategies for designing wet/composite anodes are summarized in Figure S26 (Supporting Information).

SEM images support these observations. Surface images show that cAl-Si_LB and cuSi_LB form dense interfaces without visible gaps (Figure S27, Supporting Information). Cross-sectional SEM reveals that LBHI-based anodes are thinner than their LPSClbased counterparts, providing better volumetric energy density (Figure S28, Supporting Information). Cyclic voltammetry (CV) and EIS analyses, conducted in full-cell configurations, elucidate the advantages of composite anodes—featuring 3D active material-SE interfaces—over wet anodes, which form 2D interfaces. The CV curve of sAl-Si (Figure \$29, Supporting Information) exhibits steeper current increases at high voltage compared to composite anodes (cAl-Si_LP and cAl-Si_LB), suggesting limited Li-ion transport in the wet configuration. EIS spectra (Figure 5g,h) further revealed that composite anodes consistently exhibit lower interfacial resistance than wet anodes due to increased contact area. Notably, the sµSi wet anode shows no xaxis intercept on the Nyquist plot, implying poor contact.

Interestingly, composite anodes with LBHI exhibited lower interfacial resistance than their LPSCl-based counterparts (Figure 5g,h), despite LBHI's lower intrinsic ionic conductivity (Figure \$30, Supporting Information). Specifically, the x-axis intercepts in the Nyquist plots for symmetric SUS||SUS cells at equal areal loadings were \approx 85–90 Ω for LBHI, compared to \approx 6.0– 6.5Ω for LPSCl, indicating more than a tenfold difference. This counterintuitive result suggests that ionic conductivity alone has a limited impact on determining the interface resistance with the active material, and the mechanical compliance of the SE plays a critical role. To evaluate the mechanical properties of the SEs used as anolytes, nanoindentation measurements were conducted under vacuum using a maximum load of 5 mN (Figure S31a-c, Supporting Information). The displacement-load profiles (Figure 5b) revealed that LPSCl and LBHI exhibited total deformations of 1.39 and 2.00 μm , respectively. This load was selected to approximate the displacement scale experienced by SEs during lithiation-induced expansion of micrometer-sized active materials such as Si. Upon load release, LPSCl retained its full deformation, indicating plastic behavior, whereas LBHI showed substantial elastic recovery, returning to 0.45 µm of residual deformation—corresponding to a recovery rate of ≈77.5%. At a reduced load of 500 μ N, the trend persisted (Figure S31d,e, Supporting Information): LBHI deformed to 416 nm and recovered more than half, while LPSCl deformed to 283 nm with minimal recovery. LBHI possesses a lower elastic modulus (21.4 GPa) and hardness (1.7 GPa) than LPSCl (83.7 and 2.4 GPa, respectively) (Figure S31f,g, Supporting Information). These behaviors suggest that LBHI exhibits resilient properties, while LPSCl behaves plastically under comparable stress conditions. These mechanical characteristics—particularly the ability to elastically recover from strain—are essential for accommodating the volumetric changes of Si-based active materials and sustaining robust interfacial contact throughout cycling. Internal stress evolution during charge-discharge cycling was evaluated in full-cell configurations with different anode types, as shown in Figure 5c,d, and

Figure S32a-f (Supporting Information). To ensure a fair comparison, all cells were fabricated with identical active material loadings: Al-Si and µSi anodes were prepared with areal loadings of 3.95 $mg_{Al\text{-}Si}$ $\cdot cm^{-2}$ and 1.79 mg_{uSi} $\cdot cm^{-2}$, respectively, while the NCM811 cathode was fixed at 25 mg_{NCM} cm⁻². These measurements aimed to investigate how anode composition and architecture affect internal mechanical stress during electrochemical cycling. Overall, anodes based on Al-Si exhibited lower internal stress variations than those using μSi . This is attributable to the intrinsically smaller volume change of Al-Si alloys during lithiation and delithiation compared to pure µSi. Interestingly, composite anodes incorporating LBHI exhibited larger stress fluctuations than those with LPSCl. This behavior likely stems from the elastic nature of LBHI, which does not undergo plastic deformation to the same extent as LPSCl. As a result, mechanical stress generated by active material expansion is more directly transferred to the cell stack without being dissipated by permanent deformation. Additionally, wet anodes exhibited lower pressure changes per unit capacity compared to composite anodes. Unlike wet anodes, where most contact points exist between active material particles, composite anodes form more extensive contact between the active material and the electrolyte. This results in a larger electrochemically active area, contributing to greater stress variations during charge-discharge cycling.[31] To investigate the electrochemical characteristics of various anode configurations, NCM full-cells were fabricated with identical anode active material loadings and evaluated through dQ/dV analysis, EIS, and self-charging/discharging measurements. The dQ/dV curves (Figure 5e,f) reveal distinct lithiation/delithiation behaviors depending on the anode type. Al-Si-based anodes showed lithiation onset near 3.29-3.34 V (vs Li/Li+) and delithiation ≈3.71–3.88 V (vs Li/Li⁺). µSi-based anodes exhibited higher lithiation/delithiation voltages (3.40-3.47 and 3.86-3.96 V vs Li/Li⁺). The higher lithiation and delithiation voltages observed in µSi anodes are attributed to the absence of Al, as the presence of Al in Al–Si anodes modulates the reaction voltage with Li. Across both active material types, LBHI-based anodes consistently exhibited higher lithiation onset and lower delithiation voltages. This behavior originates from a previous computational study,[31] which revealed that LBHI possesses a low electrochemical reaction energy with Si-based anode materials and ionic conductivity, thereby resulting in higher overpotentials for the reactions to proceed. Impedance spectroscopy (Figure \$33, Supporting Information) further elucidated interfacial behavior. cAl-Si_LB showed the smallest semicircles at both SOC 100% and SOD 100%, indicating the lowest charge-transfer resistance and stable interfacial contact throughout cycling. µSi-based anodes exhibited higher charge-transfer resistance than their Al–Si counterparts. Notably, sµSi failed to establish defined x-axis intercepts on the Nyquist plot, even after cycling, confirming poor interfacial contact. EIS analysis after 100 cycles (Figure \$34, Supporting Information) further confirmed these observations Al-Si-based composite anodes (cAl-Si_LB and cAl-Si_LP) maintained low interfacial and charge-transfer resistance, with only a slight increase, whereas wet anodes and µSi-based composite anodes exhibited substantially increased resistance. Compared to the as-pressed anode surfaces in Figure S27 (Supporting Information), the anodes suffered noticeable degradation during 100 cycles, including pore formation, as shown in Figure S35 (Supporting Information).

16163028, 2025, 43, Downloaded from https://advanced.onlinelibrary.wiley.com/ab/10.1002/adfm.202504739 by Dagau Gyeongbuk Institute Of, Wiley Online Library on [03/12/2025]. See the Terms and Conditions (https://onlinelibrary.wiley.

and-conditions) on Wiley Online Library for rules of use; OA articles are governed by the applicable Creative Commons

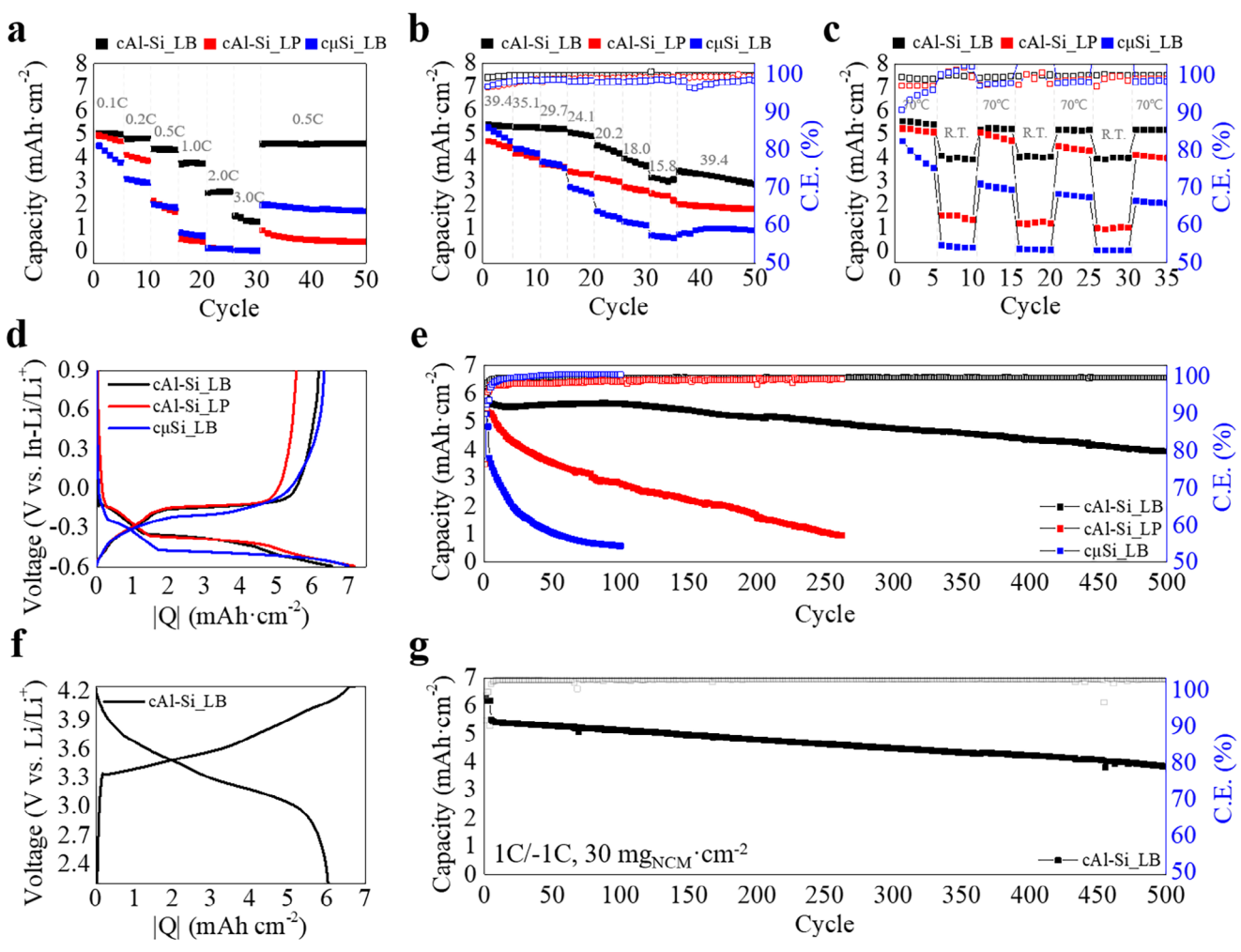


Figure 6. Cell performance for In-Li half-cells and NCM811 full-cell. a) Rate performance of In-Li half-cells. b) Stack pressure dependency test for In-Li half-cells, c) Temperature sensitivity of In-Li half-cells under varying operation temperatures (70 °C to R.T.), d) Voltage profiles, and e) cycle life of In-Li half-cells operating at 0.2C. f,g) Voltage profile and cycling performance of an NCM811 full cell with a cAl-Si_LB anode.

Nevertheless, the anodes with Al-Si as active materials maintained dense contact between the active material and SEs due to the softness of the material and lower volume variation. In contrast, clear boundaries between the active material and the SE were observed in the µSi anodes. Notably, for the sµSi, significant cracking was observed, in stark contrast to the exceptionally smooth surface of the sAl-Si electrode.

Self-charging/discharging behavior was assessed via 10 h rest periods at 4.25 and 2.2 V (vs Li/Li+) to prove long-term stability (Figure 5i,j; Figure \$36, Supporting Information). cAl-Si_LB showed the smallest voltage drift, indicating superior electrochemical stability across both high and low voltage ranges. To further examine the interfacial chemical evolution, XPS analysis was performed on the solid electrolytes within Al-Si composite anodes before and after cycling (Figure \$37, Supporting Information). In the LPSCl-based system, distinct signals corresponding to Li₂S and Li₃P—known decomposition products of LPSCl-were observed after ten cycles, indicating ongoing interfacial reactions.[10,13,49] In contrast, the LBHI-based system showed no significant changes in chemical composition before and after cycling, aside from minor oxidation peaks in the B 1s region.[31,50,51] These peaks are attributed to air exposure during sample transfer rather than electrochemical degradation.

2.5. High Loading Cell Performance

To evaluate the performance of ASSBs with different anode configurations, In-Li half-cells were tested under varying C-rates, stack pressures, and temperatures. The assessments also included cell longevity. All cells used consistent active material loadings to enable fair comparison between wet and composite anodes. Specifically, the Al-Si and µSi anodes were loaded at 3.95 mg_{Al-Si}·cm⁻² and 1.79 mg_{uSi}·cm⁻², respectively. Precycling involved one cycle at 0.05C followed by three cycles at 0.1C, with the final capacity used as a baseline.

Rate capability was tested from 0.1 to 3C at 70 °C under 39.4 MPa, with five cycles per rate (Figure 6a; Figure S38, Supporting Information). The cAl-Si_LB cell delivered 5 mAh·cm⁻² at 0.1C and retained ≈75% capacity at 1C, demonstrating robust





www.afm-journal.de

operation with substantial capacity retention. In contrast, cAl–Si_LP started at 4.81 mAh·cm $^{-2}$ at 0.1C but retained only 81.9% at 0.2C, with a sharp capacity drop beyond 0.5C, indicating its limited rate capability. The cµSi_LB anode exhibited steady capacity decline even at low rates and underperformed compared to cAl–Si_LP, though its capacity stabilized above 0.5C, likely due to constrained Si expansion. After 3C testing, rate recovery at 0.5C showed cAl–Si_LB retained $\approx\!4.5$ mAh·cm $^{-2}$, while cµSi_LB and cAl–Si_LP retained $>\!2$ and $<\!1$ mAh·cm $^{-2}$, respectively, with signs of continuous degradation. In extended cycling at 0.5C for 120 cycles (Figure S39, Supporting Information), cAl–Si_LB remained stable at 4.3–4.6 mAh·cm $^{-2}$, whereas cµSi_LB declined from 2 to $\approx\!1$ mAh·cm $^{-2}$.

cµSi_LP initially delivered 3.5–5.0 mAh·cm⁻² at 0.1C (Figure S38b, Supporting Information) but significantly declined beyond 0.2C. In comparison, wet anodes showed significant limitations under high loading (Figure S38a,c, Supporting Information). The wet anodes exhibited low ICE and poor cycling stability, with capacities of 3.0–3.5 and 1.0–2.0 mAh·cm⁻² at 0.1C, respectively, and $< 1~\text{mAh·cm}^{-2}$ at higher rates.

The effect of stack pressure on the capacity of In-Li half-cells with different anodes was evaluated over five cycles at 0.1 and 70 $^{\circ}$ C (Figure 6b; Figure S40, Supporting Information). Using torque wrenches, the torque was incrementally reduced in steps of 5 N·m, corresponding to a decrease in calibrated stack pressure from 39.4 to 15.8 MPa.

The cAl-Si_LB retained 93.5% capacity (from 5.3 mAh·cm⁻²) down to 24.1 MPa, but dropped significantly at 15.8 MPa, though still outperforming other cells. In contrast, cuSi_LB dropped rapidly below 29.7 MPa. While cAl-Si_LP showed continuous decline with decreasing pressure, the cuSi_LP followed a similar but more severe trend. Nevertheless, both wet anodes were more susceptible to variations in stack pressure at equivalent loading levels of active materials compared to composite anodes, reflecting their inherent structural and interfacial weaknesses. Across all anodes, the capacity loss resulting from reduced stack pressure was not fully recoverable, even when the pressure was restored to 39.4 MPa, suggesting irreversible mechanical or interfacial degradation. These results highlight that the practical application of Si-based alloys as anodes operating without external pressure remains challenging, even with the support of selfhealing analytes and active materials designed for low volume variation.

To assess the temperature dependence and versatility of operation, charge-discharge cycling of In-Li half-cells with different anodes was conducted at 0.1C under 39.4 MPa, alternating between 70 °C and room-temperature (R.T.) over five cycles (Figure 6c; Figure S41, Supporting Information). The cAl-Si_LB delivered 5.2–5.5 mAh·cm⁻² at 70 °C and retained 73–77% at R.T. (≈4 mAh·cm⁻²). In contrast, cAl-Si_LP dropped from 4.0-5.2 to 1.0–1.5 mAh·cm⁻² (25–29%) at R.T., suggesting that the Al– Si/LPSCl system is more sensitive to temperature than the LBHIbased counterpart. Both cuSi_LB and cuSi_LP, as well as the wet anodes, exhibited negligible capacity at R.T. Despite LPSCl's ionic conductivity being an order of magnitude higher than LBHI (as measured in SUS||SUS EIS cells),[31] cAl-Si_LB performed better at R.T., implying that other factors—mechanical properties, contact quality, or electrochemical compatibility—also influence performance. To further investigate the temperature dependency of each electrode, full-cells were analyzed by EIS over 80-20 °C, in 5 °C increments (Figure S42, Supporting Information). Lower temperatures caused increased resistance in all cells, particularly for uSi-based anodes. Incomplete x-axis intersection in EIS plots suggests poor interfacial contact at low temperatures. The cycle life of In-Li half-cells was evaluated for each electrode under operating conditions of 70 °C and 39.4 MPa. Precycling was performed prior to the main cycles, beginning with one cycle at 0.05C with a cut-off voltage range of -0.595 to 0.9 V, followed by three cycles at 0.1C with a cut-off voltage range of -0.59 to 0.6 V. ICE values were 94.5% (cAl-Si_LB), 77.5% (cAl-Si_LP), and 56.9% (sAl-Si); and 90.3% (cµSi_LB), 86.9% (cµSi_LP), 85.2% (sµSi) (Figure 6d; Figure \$43, Supporting Information). Regardless of the active material, composite anodes consistently exhibited higher ICEs compared to wet anodes. Moreover, the use of LBHI as an analyte contributed to enhanced ICE compared to the LPSCl anolyte. Cycle life evaluations at 0.2C revealed significant differences in performance among the anodes. The cAl-Si_LB maintained its initial capacity after 100 cycles and retained over 70% of its capacity after 500 cycles (Figure 6e). In contrast, the cAl-Si_LP, sAl-Si, cµSi_LB, cµSi_LP, and sµSi experienced rapid capacity declines, dropping to 2 mAh·cm⁻² after 177, 91, 21, 20, and 8 cycles, respectively (Figure 6e; Figure S43, Supporting Information).

To assess the feasibility of full-cell operation using highloading cathodes paired with the high-performing cAl-Si_LB anodes, and to optimize full-cell conditions, we conducted a comprehensive evaluation encompassing C-rate performance, negative-to-positive capacity (N/P) ratio optimization, highloading configurations, and long-term cycling stability. For rate capability testing, full cells were assembled using an NCM dry cathode with a loading of 30 mg_{NCM}·cm⁻² and a cAl-Si_LB anode at 5.54 mg_{Al-Si}·cm⁻² (Figure S44a,b, Supporting Information). Cells were cycled sequentially from 0.1 to 3C with five cycles per rate, followed by a return to 0.2C. The rate performance closely mirrored trends observed in In-Li half-cells. At 0.1C, the full-cell delivered an areal capacity of \approx 6.7 mAh·cm⁻², with 81.4% of this capacity retained at 1C, indicating excellent rate capability. To determine the optimal N/P ratio, anode loadings were varied between 5.1 and $9.2~\text{mg}_{\text{NCM}}\cdot\text{cm}^{-2}$ while maintaining similar cathode loadings. ICEs ranged from 87-90%, with a peak ICE of 89.5% achieved at 5.54 mg_{NCM}·cm⁻², designating this configuration as optimal (Figure S44c, Supporting Information). From the measured areal capacities—7.13 mAh·cm⁻² for the anode (5.54 $mg_{\text{Al-Si}}\ cm^{--2})$ and 6.06 mAh cm^{-2} for the cathode (30 $\rm mg_{NCM} \cdot cm^{-2})$ —the full-cell N/P ratio was calculated to be 1.18 (Figure \$45, Supporting Information). The corresponding volumetric and gravimetric energy densities were 262.6 Wh·L⁻¹ and 118.1 Wh·kg⁻¹, respectively (Table \$3, Supporting Information). The laboratory setup employed a relatively thick LPSCl layer via cold pressing without dry-room or WIP equipment, contributing 72.2% of total cell volume and 64.6% of mass. If replaced with a commercially feasible thin SE layer (< 50 µm), energy densities could reach 760.8 Wh·L⁻¹ and 283.4 Wh·kg⁻¹. Cycling stability was evaluated using the optimized N/P ratio under a stack pressure of 58.6 MPa and cycling rates of 0.5 and 1.0C (Figure 6f,g; Figure \$46, Supporting Information). After precycling, the initial 0.05C cycle yielded a reversible capacity of 6.02 mAh·cm⁻² with an ICE of 89.2%. At 0.5C, capacity started



www.afm-journal.de

at 5.95 mAh·cm $^{-2}$ and retained \approx 80% after 300 cycles. Under 1C conditions, 5.51 mAh·cm⁻² was delivered initially, with 81.6% retention after 300 cycles and ≈70% after 500 cycles, demonstrating excellent cycling stability even at elevated rates. These results highlight the excellent long-term cycling stability and robustness of the high-loading cAl-Si_LB configuration, even under elevated rates. To investigate the source of capacity fading, cross-sectional SEM/EDS analysis was performed on cells after 5 and 10 cycles (Figure S47, Supporting Information). Despite the elastic recovery behavior of the LBHI anolyte, repeated cycling led to partial residual deformation and gradual formation of interfacial voids between Al-Si particles and LBHI. This progressive contact loss was identified as the main degradation mechanism, rather than pulverization of the active material or electrolyte decomposition. To expand this evaluation, full cells were assembled with NCM cathodes at 45, 78, and 180 mg_{NCM}·cm⁻² (Figure S44d,e, Supporting Information). Corresponding Al-Si anode loadings were 8.3, 14.4, and 33.2 mg_{Al-Si}·cm⁻². All cells were cycled under 58.6 MPa at 70 °C. Precycling was performed at 0.05C for the 45 mg_{NCM}·cm⁻² cell and 0.02C for the higher-loading cells. Lifespan evaluations followed at 0.1, 0.05, and 0.02C, depending on loading, with a limited number of cycles used to determine feasibility. ICEs ranged from 87-92%, consistent with those of 30 mg_{NCM}·cm⁻² cathodes, confirming that high initial efficiency is retained even at higher loadings. The reversible capacities of the 45, 78, and 180 mg_{NCM}·cm⁻² cathodes were 9.49, 16.16, and 36.54 mAh⋅cm⁻², respectively. All showed stable capacity retention beyond ten cycles, demonstrating that high-loading electrodes can deliver significantly enhanced capacities while maintaining cycling efficiency.

A comparative analysis was conducted to systematically evaluate the electrochemical performance of Al-Si alloys against stateof-the-art Si-based anodes in ASSBs. The electrochemical performance of ASSBs is summarized in Tables for a comprehensive comparison. Table S4 (Supporting Information) presents data on ASSBs utilizing Si-based anodes (without prelithiation) paired with NCM cathodes. The table outlines key parameters, including active material, ICE, areal capacity, C-rate for the main cycle, cycle count, and cycle retention. From the 14 studies compared in Table S4 (Supporting Information), cAl-Si_LB demonstrated superior ICE and cycling performance at high areal capacity and C-rate, establishing itself as a well-rounded anode. While SE-free Si anodes are known to enable higher loadings and simpler processing, [10,13] the composite anodes with embedded SEs investigated in this study demonstrated superior performance in terms of rate capability, stack pressure tolerance, temperature stability, and cycling durability. Composite anodes support more robust electrode architectures—allowing for high loading, reduced dependence on external pressure and temperature-ultimately outweighing their limitations.^[52] With the development of a stable, non-reactive binder suitable for sulfide-based ASSBs, incorporating SEs into the anode becomes a practical and reliable strategy for real-world applications.

3. Conclusion

This study presents a comprehensive approach to advancing Si anodes in sulfide-based ASSBs, emphasizing stepwise improvements in material design and compatibility strategies. The re-

search highlights the progression from pure Si anodes to Al–Si and prelithiated Al–Si, while proposing practical solutions for applying wet anodes to ASSBs. A key insight from this work is the need to minimize electrode volume changes to preserve stable contact at the 2D interface between the anode and SE.

However, the limitations of this planar interface are also highlighted, with composite anodes forming a 3D interface proposed as a more effective alternative. The study further emphasizes the importance of mechanical and electrochemical compatibility between SEs and active materials in achieving long-term cycling stability. By leveraging these design principles, ASSBs incorporating Al–Si anodes and LBHI electrolytes demonstrated outstanding capacity retention of 81.6% after 300 cycles at an areal capacity of 6 mAh·cm $^{-2}$. This work underscores the potential of engineered anode–electrolyte architectures to address persistent challenges in ASSB development, offering a promising route toward the practical realization of high-energy-density ASSBs.

Supporting Information

Supporting Information is available from the Wiley Online Library or from the author.

Acknowledgements

This work was supported by the Materials and Components Technology Development Program of MOTIE/KEIT (Grant No. 20007045) and the National Research Foundation of Korea (NRF) grant funded by the Korea government (MSIT) (No. 2021R1A2B5B03001416). Nano-CT was performed at the 7C beamline of the Pohang Accelerator Laboratory.

Conflict of Interest

The authors declare no conflict of interest.

Author Contributions

S.Y., S.C., and S.K. contributed equally to this work. S.Y. and S.C. proposed this research. S.K. and Y.S. conducted a numerical volume expansion simulation. I.N. and J.L. conducted the full-cell optimization and analyzed the data. All authors discussed and analyzed the data. S.Y., S.C., and S.K. contributed to the writing and revision of the manuscript. S.Y., S.C., and S.K. equally contributed. Y.M.L. and S.P. guided the whole project.

Data Availability Statement

The data that support the findings of this study are available from the corresponding author upon reasonable request.

Keywords

all-solid-state batteries, anolytes, electro-chemo-mechanics, silicon-based anodes, sulfide solid electrolytes

Received: February 21, 2025 Revised: April 29, 2025 Published online: May 9, 2025

and Conditions

for rules of use; OA

by the applicable Creative Common

ADVANCED
FUNCTIONAL
MATERIALS

- [1] Y. G. Lee, S. Fujiki, C. Jung, N. Suzuki, N. Yashiro, R. Omoda, D.-S. Ko, T. Shiratsuchi, T. Sugimoto, S. Ryu, J. H. Ku, T. Watanabe, Y. Park, Y. Aihara, D. Im, I. T. Han, *Nat. Energy* 2020, 5, 299.
- [2] Y. K. Sun, ACS Energy Lett. 2020, 5, 3221.
- [3] H. Li, T. Yamaguchi, S. Matsumoto, H. Hoshikawa, T. Kumagai, N. L. Okamoto, T. Ichitsubo, Nat. Commun. 2020, 11, 1584.
- [4] M. N. Obrovac, V. L. Chevrier, Chem. Rev. 2014, 114, 11444,.
- [5] J. Y. Kim, S. Jung, S. H. Kang, J. Park, M. J. Lee, D. Jin, D. O. Shin, Y.-G. Lee, Y. M. Lee, Adv. Energy Mater. 2022, 12, 2103108
- [6] D. Cao, X. Sun, Y. Li, A. Anderson, W. Lu, H. Zhu, Adv. Mater. 2022, 34, 2200401.
- [7] S. Lee, K.-S. Lee, S. Kim, K. Yoon, S. Han, M. H. Lee, Y. Ko, J. H. Noh, W. Kim, K. Kang, Sci. Adv. 2022, 8, abq0153.
- [8] F. Boorboor Ajdari, P. Asghari, A. Molaei Aghdam, F. Abbasi, R. P. Rao, A. Abbasi, F. Ghasemi, S. Ramakrishna, N. Mikaeili Chahartagh, Adv. Funct. Mater. 2024, 34, 2314822.
- [9] S. Y. Han, C. Lee, J. A. Lewis, D. Yeh, Y. Liu, H. W. Lee, M. T. McDowell, Joule 2021, 5, 2450.
- [10] D. H. S. Tan, Y. T. Chen, H. Yang, W. Bao, B. Sreenarayanan, J. M. Doux, W. Li, B. Lu, S. Y. Ham, B. Sayahpour, J. Scharf, E. A. Wu, G. Deysher, H. E. Han, H. J. Hah, H. Jeong, J. B. Lee, Z. Chen, Y. S. Meng, Science 2021, 373, 1494.
- [11] J. A. Lewis, K. A. Cavallaro, Y. Liu, M. T. McDowell, Joule 2022, 6, 1418
- [12] H. Huo, M. Jiang, Y. Bai, S. Ahmed, K. Volz, H. Hartmann, A. Henss, C. V. Singh, D. Raabe, J. Janek, Nat. Mater. 2024, 23, 543.
- [13] W. Yan, Z. Mu, Z. Wang, Y. Huang, D. Wu, P. Lu, J. Lu, J. Xu, Y. Wu, T. Ma, M. Yang, X. Zhu, Y. Xia, S. Shi, L. Chen, H. Li, F. Wu, Nat. Energy 2023, 8, 800.
- [14] M. Grandjean, M. Pichardo, Y. Biecher, C. Haon, P. Chenevier, J. Power Sources 2023, 580, 233386.
- [15] X. Xu, Q. Sun, Y. Li, F. Ji, J. Cheng, H. Zhang, Z. Zeng, Y. Rao, H. Liu, D. Li, L. Ci, Small 2023, 19, 2302934.
- [16] M. So, T. Yano, A. Permatasari, V. L. Nguyen, G. Inoue, Adv. Funct. Mater. 2025, https://doi.org/10.1002/adfm.202423877.
- [17] S.-Y. Ham, E. Sebti, A. Cronk, T. Pennebaker, G. Deysher, Y.-T. Chen, J. A. S. Oh, J. B. Lee, M. S. Song, P. Ridley, D. H. S. Tan, R. J. Clément, J. Jang, Y. S. Meng, *Nat. Commun.* **2024**, *15*, 2991.
- [18] Z. Zhang, Z. Sun, X. Han, Y. Liu, S. Pei, Y. Li, L. Luo, P. Su, C. Lan, Z. Zhang, S. Xu, S. Guo, W. Huang, S. Chen, M. S. Wang, *Energy Environ. Sci.* 2024, 17, 1061.
- [19] Z. Fan, B. Ding, Z. Li, Z. Chang, B. Hu, C. Xu, X. Zhang, H. Dou, X. Zhang, eTransportation 2023, 18, 100277.
- [20] L. Cui, S. Zhang, J. Ju, T. Liu, Y. Zheng, J. Xu, Y. Wang, Nat. Energy 2024, 9, 1084.
- [21] J. Sung, S. Y. Kim, A. Harutyunyan, M. Amirmaleki, Y. Lee, Y. Son, J. Li, Adv. Mater. 2023, 35, 2210835.
- [22] G. J. Lee, D. Lee, S. H. Choi, C. H. Baek, J. Y. Jung, W. Cho, W. S. Yoon, D. J. Yoo, J.-S. Yu, ACS Energy Lett. 2024, 9, 3807.
- [23] L. A. Berla, S. W. Lee, Y. Cui, W. D. Nix, J. Power Sources 2015, 273, 41.
- [24] J. Cai, X. Zhang, H. Gou, G. Wang, ACS Energy Lett. 2025, 10, 439.
- [25] C. Xu, S. Sun, J. Zhao, X. Zhang, X. Feng, S. A. T. Redfern, C. Xia, H. Gou, G. Wang, *Acta Mater.* 2025, 283, 120570.

- [26] Y. Liu, C. Wang, S. G. Yoon, S. Y. Han, J. A. Lewis, D. Prakash, E. J. Klein, T. Chen, D. H. Kang, D. Majumdar, R. Gopalaswamy, M. T. McDowell, Nat. Commun. 2023, 14, 3975.
- [27] G. Hwang, H. Park, T. Bok, S. Choi, S. Lee, I. Hwang, N. S. Choi, K. Seo, S. Park, Chem. Commun. 2015, 51, 4429.
- [28] J. Ding, J. Sun, B. Ban, X. Jiang, X. Zhu, Z. Mo, L. Wang, J. Chen, 2024, Silicon, 16, 4479.
- [29] B. Ding, Z. Cai, Z. Ahsan, Y. Ma, S. Zhang, G. Song, C. Yuan, W. Yang, C. Wen, Acta Metallurgica Sinica 2021, 34, 291.
- [30] A. Pisch, N. Jakse, A. Pasturel, J. P. Harvey, P. Chartrand, Appl. Phys. Lett. 2007, 90, 251902.
- [31] Y. Huang, B. Shao, Y. Wang, F. Han, Energy Environ. Sci. 2023, 16, 1569.
- [32] X. Xiong, T. Lin, C. Tian, G. Jiang, R. Xu, H. Li, L. Chen, L. Suo, Nat. Commun. 2024, 15, 3706.
- [33] Y. Wang, Y. Lu, J. Zhang, W. Yang, C. Yang, P. Wang, X. Song, Z. Chen, Mater. Sci. Technol. 67, 186.
- [34] W. Cao, K. Han, M. Chen, H. Ye, S. Sang, Electrochim. Acta 2019, 320, 134613.
- [35] K. Wang, Y. Tan, P. Li, J. Sun, Electrochim. Acta 2020, 353, 136538.
- [36] J. Sun, J. Li, B. Ban, J. Shi, Q. Wang, J. Chen, Electrochim. Acta 2020, 345, 136242.
- [37] N. Saini, D. K. Dwivedi, P. K. Jain, H. Singh, Procedia Eng. 2015, 100, 1522.
- [38] M. D. Fleischauer, M. N. Obrovac, J. R. Dahn, J. Electrochem. Soc. 2008, 155, A851.
- [39] F. Fuchs, M. Bilal Khan, D. Deb, D. Pohl, J. Schuster, W. M. Weber, U. Mühle, M. Löffler, Y. M. Georgiev, A. Erbe, S. Gemming, J. Appl. Phys. 2020, 128, 085301.
- [40] C. Rarey, J. Stringer, J. Edington, Trans. Met. Soc. AIME 1966, 236, 811.
- [41] S. Kim, H. Lee, J. Lim, J. Park, Y. M. Lee, ACS Energy Lett. 2024, 9, 5225
- [42] J. Song, S. H. Lim, K. G. Kim, N. Umirov, H. Lee, C. B. Dzakpasu, J. Lim, J. Nam, J. Park, J.-N. Lee, H. Munakata, K. Kanamura, S. S. Kim, Y. M. Lee, Adv. Energy Mater. 2023, 13, 2204328.
- [43] J. Zhu, J. Luo, J. Li, S. Huang, H. Geng, Z. Chen, L. Jia, Y. Fu, X. Zhang, X. Zhuang, Adv. Mater. 2024, 36, 2407128.
- [44] D. E. Arreaga-Salas, A. K. Sra, K. Roodenko, Y. J. Chabal, C. L. Hinkle, J. Phys. Chem. C 2012, 116, 9072.
- [45] K. Han, J. Shen, C. M. Hayner, H. Ye, M. C. Kung, H. H. Kung, J. Power Sources 2014, 251, 331.
- [46] D. Wu, J. Peng, Z. Jiang, L. Zhu, Y. Wu, C. Xu, Z. Wang, M. Yang, H. Li, L. Chen, F. Wu, Energy Storage Mater. 2024, 72, 103749.
- [47] S. Cangaz, F. Hippauf, F. S. Reuter, S. Doerfler, T. Abendroth, H. Althues, S. Kaskel, Adv. Energy Mater. 2020, 10, 2001320.
- [48] A. Mazzucco, E. M. Dematteis, V. Gulino, M. Corno, M. F. Sgroi, M. Palumbo, M. Baricco, RSC Adv. 2024, 14, 12038.
- [49] J. Kim, W. Choi, S. J. Hwang, D. W. Kim, Energy Environ. Mater. 2024, 7, 12776.
- [50] Q. Zhang, F. H. Li, X. X. Zhang, H. B. Wang, F. C. Li, Z. Y. Guo, Z. Zhang, J. Electrochem. Soc. 168, 040522.
- [51] B. J. Matsoso, V. Vuillet-a-Ciles, L. Bois, B. Toury, C. Journet, Nanomaterials 2020, 10, 443.
- [52] H. Pan, L. Wang, Y. Shi, C. Sheng, S. Yang, P. He, H. Zhou, Nat. Commun. 2024, 15, 2263.